Chapter 3

Low Temperature Plasma Nitriding of Austenitic Stainless Steels

Tatsuhiko Aizawa

Additional information is available at the end of the chapter

http://dx.doi.org/10.5772/intechopen.78365

Abstract

A low temperature plasma nitriding process has become one of the most promising methods to make solid-solution hardening by the nitrogen super-saturation, being free from toxicity and energy consumption. High-density radio-frequency and direct current (RF/DC) plasma nitriding process was applied to synthesize the nitrided AISI304 microstructure and to describe the essential mechanism of inner nitriding in this low temperature nitriding (LTN) process. In case of the nitrided AISI304 at 673 K for 14.4 ks, the nitrided layer thickness became 66.5 μm with the surface hardness of 1550 HV and the surface nitrogen content of 9 mass%. This inner nitriding process was governed by the synergetic interrelation among the nitrogen super-saturation, the lattice expansion, the phase transformation, the plastic straining, the microstructure refinement, and the acceleration of nitrogen diffusion. When this interrelation is sustained during the nitriding process, the original austenitic microstructure is homogeneously nitrided to have fine-grained microstructure with the average size of 0.1 μm. Once this interrelation does not work anymore, the homogeneous microstructure changed itself to the heterogeneous one. The plastic straining took place in the selected coarse grains so that the parts of them were only refined. This plastic localization accompanied with the localized phase transformation.

Keywords: high-density plasma nitriding, low holding temperature (T_H), nitrogen super-saturation, γ-lattice expansion, phase transformation, elastic strain distortion, plastic straining, microstructure refinement, nitrogen diffusion path

1. Introduction

Iron-nitrogen or Fe-N binary system is essential in the steel design in a similar manner to the iron-carbon system [1]. Since the maximum solubility limit of nitrogen solutes is only 0.1

mass% or 0.3 at%, most of the previous studies concentrated on the solubility of nitrogen into γ-phase at a higher temperature than 1000 K [2]. Under those research circumstances, three important items in the material science were pointed out as findings to be noticed. Nitrogen works as a γ-phase stabilizer so that phase transformation temperature from α/α′- to γ-phase decreases with increasing the nitrogen content, [N] [3]. Mechanical properties significantly improve by themselves also with increasing [N] [4]. Thirdly, a crystalline structure of nitrogen super-saturated iron or Fe (N) resembles with that of iron nitride; for example, α′-Fe (N) with the nitrogen content of 11 at% has the same crystalline structure of α″-$Fe_{16}N_2$ and γ-Fe (N) with 20 at% nitrogen solute content corresponds to γ′-Fe_4N as surveyed in the textbook [5]. The first two items stimulated further researches for high-nitrogen steels (HNS) as discussed in [6]. The third item leads to the chemical vapor deposition of $Fe_{16}N_2$ thin films on the template substrate [7].

An pressurized electro-slag remelting (ESR) method has become a standard approach to fabricate an ingot of HNS [8]. Relatively high amount of dissociated nitrogen atoms from N_2 gas can diffuse into the depth of γ-phase matrix at 1263 K. This solution nitriding method induced the nitrogen atoms even into high chromium content steels including austenitic stainless steels [9]. Through this process, the nickel resource can be saved by 69 kg only by the addition of nitrogen atoms by 1 kg. The nitrogen works to stabilize the austenitic phase even with less nickel content. These nickel-free HNS have coarse grains, resulting in embrittlement, difficulty in welding, and insufficient stability in working. Although many trials have been made to improve the nitrogen solute content higher than 1 mass%, most of the studies experienced engineering difficulties to find a new alloying effect on the increase of strength and corrosion resistance [10].

In parallel with research on HNS, ion- and radical nitriding processes were developed with the use of the direct current (DC)-plasma and DC-pulse plasma technologies [11]. The T_H was held to be higher than 900 K in them; CrN was synthesized as a precipitate in the matrix together with iron nitrides such as Fe_2N and γ′-Fe_4N [12]. Hence, the stainless steels and Fe-Cr alloys were hardened by fine precipitation of CrN; however, the chromium content in the matrix was reduced by CrN-precipitation reaction to lower the original corrosion resistance [13]. In addition, this high temperature plasma nitriding was mainly governed by the nitrogen diffusion process; the nitrogen solute content exponentially decreases from the maximum nitrogen solid solubility of 0.1 mass% at the surface down to 0 toward the nitriding front-end [14]. Furthermore, when the T_H was higher than 1000 K, the chromium also diffuses to form a multi-stripe pattern with layered structure of {- (Cr-rich) - (CrN-rich) -} during nitriding [15]. Most of engineers and companies related to plasma nitriding believe that chemical reaction of chromium with nitrogen should drive the nitrided layer formation and hardening.

British research group [16] first found the nitrogen super-saturated lattices in the austenitic stainless steels by low temperature plasma nitriding. When using the same DC or DC-pulse plasmas, the nitriding process is characterized mainly by CrN precipitation into matrix when T_H is higher than 800 K. On the other hand, an original γ-lattice expands to form a peak shift from the original peaks of austenitic stainless steels in X-ray diffraction (XRD) analysis when $T_H < 800$ K. This finding does not mean a formation of new phase, so called by S-phase, but implies that nitrogen super-saturation accompanies with the γ-lattice expansion and that the crystalline structure of

this Fe (N) is essentially different from that of original austenitic stainless steel matrix. In addition, various new engineering is expected to start from this nitrogen super-saturated Fe (N) [17].

In the present chapter, this low temperature nitriding (LTN) with nitrogen super-saturation is reconsidered by developing a new tool to drive LTN in the AISI304 stainless steels. First, Radio-frequency(RF)-DC plasma nitriding system is introduced with comments on the essential difference from other plasma nitriding processes such as DC- and DC-pulse plasmas. Quantitative plasma diagnosis equipment is stated to describe the nitrogen-hydrogen plasmas. In particular, the effect of hydrogen content in the mixture gas on the nitriding process is analyzed to determine the optimum condition. A hollow cathode device is proposed to intensify the ion and electron densities.

An austenitic stainless steel type AISI304 specimen is employed for plasma nitriding at 673 K for 14.4 ks by 60 Pa. Each fundamental process in this low temperature inner nitriding is analyzed by XRD, scanning electron microscopy (SEM)-electron dispersive X-ray spectroscopy (EDX), and electron back-scattering diffraction (EBSD). The γ-lattice expansion is analyzed as a peak shift in the XRD diagram. The nitrogen super-saturation is described by SEM-EDX; the elastic distortion is directly calculated by the lattice strain. The phase transformation, the plastic straining as well as the microstructure refinement are analyzed by EBSD. The nitrogen diffusion path is mainly estimated by the grain boundary diffusion process. These processes are mutually related to form a synergetic loop to drive this low temperature inner nitriding. When this loop is sustained during nitriding, the nitriding front-end advances homogeneously into the depth of stainless steel matrix. Once this loop is shut down at any point, the inner nitriding localizes by itself only to form a heterogeneous microstructure.

2. High-density plasma nitriding system

High-density RF-DC plasma nitriding system is introduced together with comments on the quantitative plasma diagnosis of nitrogen-hydrogen plasmas and on the hollow cathode device to intensify the ion and electron densities.

2.1. Background

DC-plasma and DC-pulse plasma [18–20] have been utilized for nitriding of stainless steel parts, tools and dies at higher hold temperature than 800 K. plasma enhanced chemical vapor deposition (PECVD) has been utilized for nitriding at lower temperature than 800 K. **Table 1** compares the difference in their capacity, inner nitriding behavior, and characteristics together with the present high-density RF-DC plasma nitriding. The former two approaches, widely utilized in the market, harden the stainless steels by CrN-precipitation and form thicker nitrided layer than 100 μm after 36 ks or 10 hours. PECVD nitriding works in the low-pressure of 1 to 2 Pa to form a moderate nitrided layer with the thickness of 20–30 μm. Inner nitriding process both in PECVD [21] and RF-DC plasma [22] is governed by nitrogen super-saturation without CrN precipitation. In the following, a detail of RF-DC plasma generation as well as a hollow cathode device is stated together with plasma diagnosis equipment in the present system.

Item	DC-Plasma （Ion Nitriding）	DC-Pulse Plasma （Radical Nitriding）	PECVD	High Density Plasma
Capacity	Large current High pressure	Small current High pressure	Small current Low pressure	Small current Marginable pressure
Holding Temperature (for SKD61)	823 K	823 K	673 – 693K	623 – 673 K
Inner Nitriding	CrN-precipitation	CrN-precipitation	Nitrogen Supersaturation	Nitrogen Supersaturation
Nitrided Layer Thickness	> 100μm for 36 ks	> 100μm for 36 ks	20—30μm for 10.8 ks	> 100μm for 14.4 ks

Table 1. Comparison of DC-plasma, DC-pulse plasma, PECVD, and RF-DC plasma nitriding processes.

2.2. RF-DC plasma nitriding system

A high-density plasma nitriding system [23–25] consisted of the vacuum chamber, the evacuation system, the DC-RF generators working in the frequency of 2 MHz, the gas supply of N_2 and H_2, and the heating unit located under the cathode plate as depicted in **Figure 1**. The nitriding parameters as well as controlling procedure are specified on the panels. All through the nitriding process, the measured pressure, temperature as well as gas pressure is automatically controlled by the process computer. Through the telecommunication, time history of RF- and DC-voltages and currents are also monitored on the panel to recognize the temporal status of RF-DC plasmas.

Figure 2 illustrates an actual experimental setup for plasma nitriding. The thermocouple is inserted into this cathode plate to monitor the T_H. In the vacuum chamber, the specimen is placed inside a hollow cathode setup on the cathode plate, which is electrically connected with DC generator. This hollow cathode setup includes a rectangle-shaped tube with the size of 40 × 20 × 70 mm^3 and the thickness of 2 mm. To be explained later, the specimen is located at the position with the highest nitrogen ion density, far half from the mixture gas inlet, as shown in **Figure 2**.

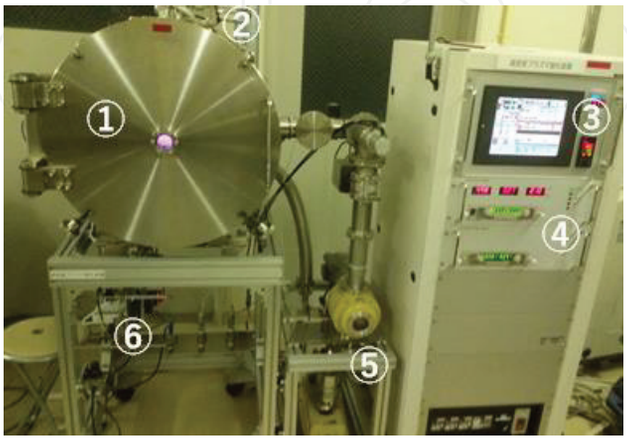

Figure 1. RF-DC plasma nitriding system. (1) Vacuum chamber, (2) RF-generator, (3) control-panel, (4) RF- and DC-power suppliers, (5) evacuation units, and (6) carrier gas supply.

http://dx.doi.org/10.5772/intechopen.78365

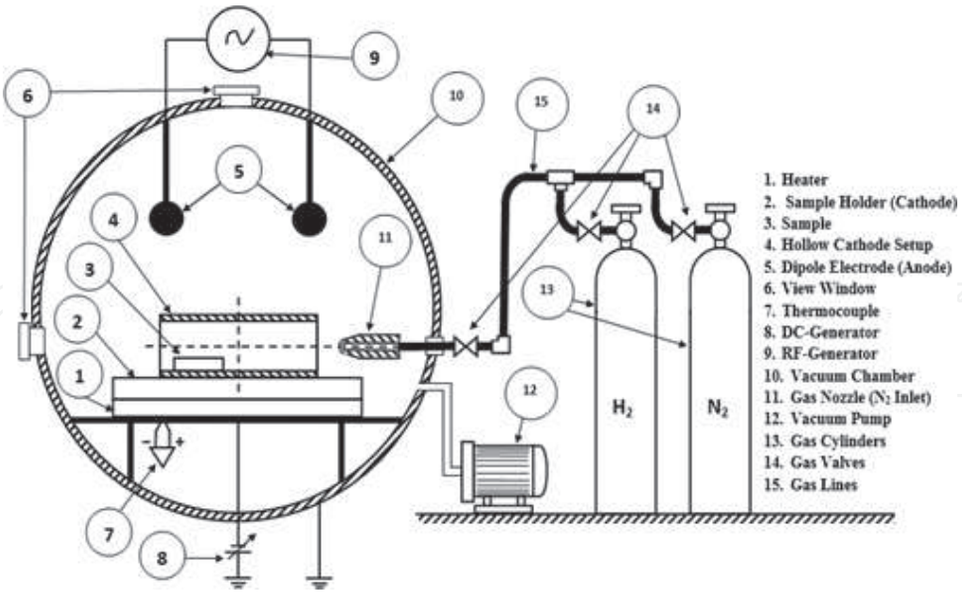

Figure 2. Experimental setup for RF-DC high-density plasma nitriding.

2.3. Quantitative plasma diagnosis

In the standard plasma diagnosis, two methods are often employed to quantitatively describe the nitrogen-hydrogen mixture plasma state; that is, emissive light optical spectroscopy (EOS) and Langmuir probe (LP). A typical setup for EOS is illustrated in **Figure 3** as precisely stated in the previous studies [26–28].

Emissive light from plasmas is detected through the optically transparent silica window on the chamber in **Figure 1** and analyzed to deduce the spectrum of species in the plasmas. **Figure 4** shows the effect of hydrogen content in the gas mixture on the measured spectra together with the spectra for hydrogen plasmas.

As seen in the spectra for hydrogen plasmas inserted in **Figure 4**, hydrogen peak intensity (Hα) at 656 nm increases monotonically with hydrogen content [H]. Pure nitrogen plasma mainly

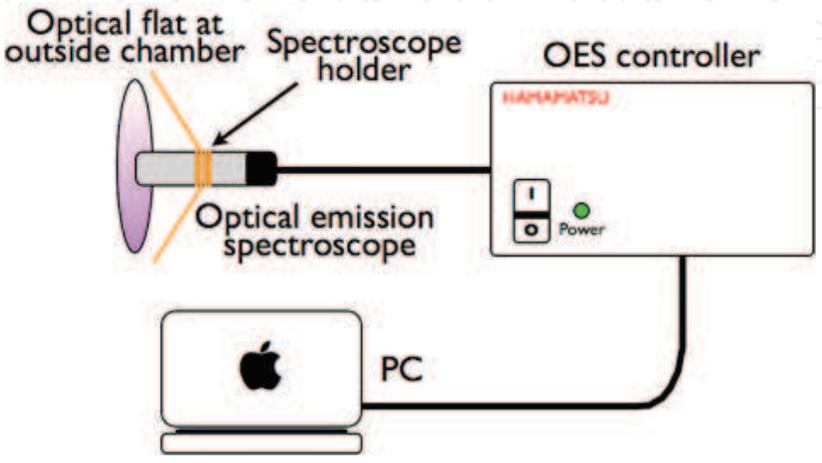

Figure 3. EOS for plasma diagnosis to describe the active species in the ignited plasmas.

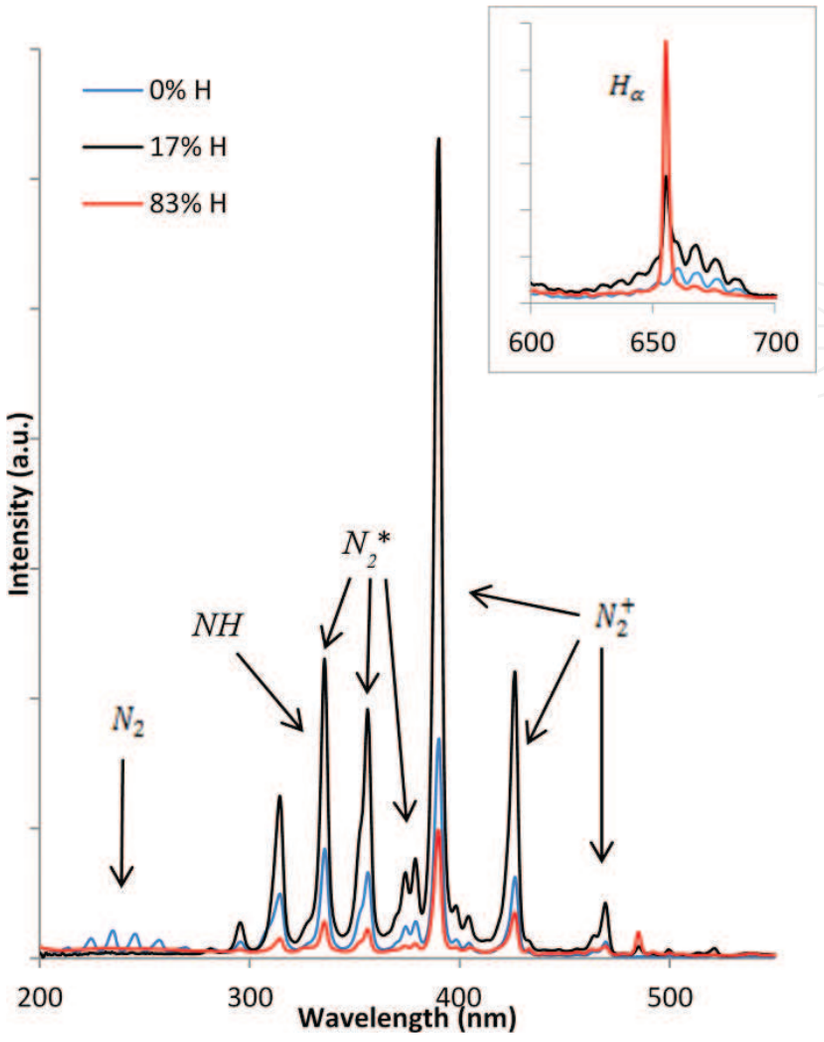

Figure 4. Measured spectra for the hydrogen-nitrogen plasmas by EOS.

consists of an excited nitrogen molecule (N_2*) and a nitrogen molecule ion (N_2^+) besides for a nitrogen molecule. When [H] = 83%, the whole population of nitrogen species including the NH-radicals significantly decreases. On the other hand, when [H] = 17%, {N_2*, N_2^+, and NH} have high-intensity without peaks for the molecular nitrogen in the range of short wavelength (<300 nm). Although the active species such as $N_2(A^3 \sum_u^+, \vartheta)$ or $N_2(X^1 \sum_g^+, \vartheta)$ cannot be observed directly from the EOS spectra, their transitions can be investigated to describe the reaction model on the active species; for example, $N_2(C^3 \prod_u \rightarrow B^3 \prod_{g^*})$ peaks observed at 337, 358, and 370 nm are related to the N_2* and $N_2^+(B^2 \sum_u^+ \rightarrow X^2 \sum_g^+)$ at 391 and 427 nm, related to the N_2^+. These second positive and the first negative bands of nitrogen play an important role in the generation of atomic nitrogen by reaction with N_2 and N_2^+ in parallel with the formation of NH-radicals as detected at 336 nm.

The LP was also utilized in the diagnosis to describe the effect of [H] on the generated plasmas. **Figure 5** depicts how to measure the ion and electron densities by using LP.

Through the direct measurement of I-V curves at the probe tip, the electron resistivity as well as the ion and electron densities are analyzed to describe the plasma state. In particular, the electron resistivity is proportional to the enhancement of plasma chemical reaction. **Figure 6**

http://dx.doi.org/10.5772/intechopen.78365

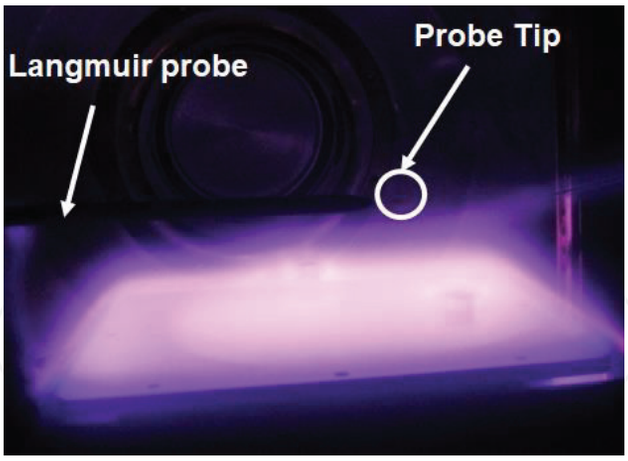

Figure 5. Experimental setups of the LP for measurement of ion and electron densities.

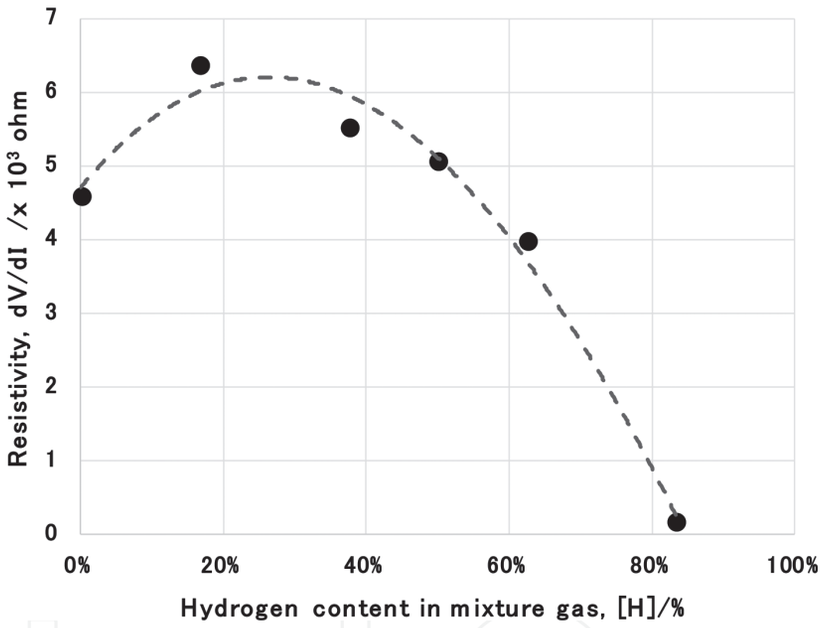

Figure 6. Variation of the measured resistivity in the plasmas with increasing the hydrogen content in the mixture gas.

shows a variation of measured resistivity in the plasmas with increasing the hydrogen content in the mixture gas.

The measured resistivity has maximum around [H] = 20–30%; a hot spot is formed in the plasmas where the chemical reaction is most enhanced for nitriding by directly controlling the hydrogen content [29].

2.4. Hollow cathode design for low temperature plasma nitriding

The hollow cathode device is utilized to intensify the ion density in the nitrogen-hydrogen plasmas. The LP is employed to directly measure the ion density in the hollow. The LP-tip was inserted into the hollow along the X-axis in every 2 cm. In each position, the tip was fixed at the center of hollow. **Figure 7** depicts the measured ion density distribution along the X-axis.

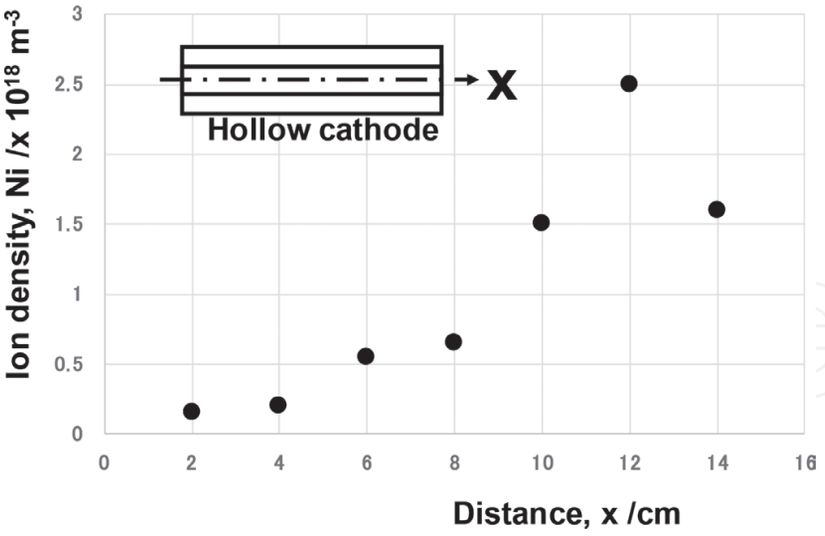

Figure 7. Measured ion density by the LP along the X-axis in the hollow.

The ion density increases monotonically with X in **Figure 7**; in particular, a hot spot with higher ion density than 1.5×10^{18} m^{-3} is located in the latter half of hollow. This is common to the hollow device effect where the ionization is enhanced at the vicinity of outlet in the hollow [30].

2.5. Observation and measurement

XRD (Rigaku SmartLab) with monochromatic Cu-Kα radiation (λ = 0.1542 nm) and Bragg–Brentano geometry, 40 kV, and 30 mA was utilized for analysis. The 2θ range was set between 30 and 90° with the scanning speed of 10 mm/min and the step angle of 0.02°. EDX device and software were utilized to make element mapping over a specified depth for nitrogen, chromium, iron, and carbon. Its spatial resolution was at most 5 μm. EBSD was utilized with the accelerating voltage of 20 kV, the working distance of 20 mm, the magnification (×2000), and the resolution of 0.1 μm. The inverse pole figure (IPF) was determined for each constituent grain to describe the change in microstructure through the nitriding. In addition, the kernel average misorientation (KAM) and the phase mapping were also measured to explain the plastic straining and phase transformation processes, respectively.

The micro-hardness testing apparatus (Mitsutoyo HM-200) was used by applying the load of 50 g or 0.5 N for hardness measurement on the cross-section in every 10 μm. The matrix hardness of AISI304 was 400 HV.

3. Low temperature plasma nitriding of austenitic stainless steels

An austenitic stainless steel type AISI304 was employed as a specimen for high-density plasma nitriding at 673 K for 14.4 ks by 60 Pa with use of the hollow cathode device. Essential processes in this low temperature plasma nitriding are described by chemical analyses.

http://dx.doi.org/10.5772/intechopen.78365

3.1. Background

An austenitic stainless steel type AISI304 was selected for plasma nitriding at lower T_H than 723 K. **Table 2** summarizes the experimental results in the literature.

Although detail information is not written in a few papers, relatively high-nitrogen surface content and formation of a nitrided layer with the thickness of 10–20 μm are common to those previous studies [31–35]. More precise analysis and discussion are needed to investigate the essential processes, governing the inner nitriding behavior at a lower temperature than 700 K. High-density RF-DC plasma systems [36–40] provides a new way to further analyze this low temperature plasma nitriding by experiments.

3.2. Nitrogen super-saturation

In the present study, AISI304 stainless steel plate with the size of 40 × 20 × 2 mm^3 was employed as a specimen for RF-DC high-density plasma nitriding at 673 K for 14.4 ks by 60 Pa for the nitrogen and hydrogen mixture gas with the flow rate ratio of 160–30 ml/min. The pre-sputtering only with the use of nitrogen gas was first performed for 1.8 ks to clean the surface condition of the specimen before nitriding. **Table 3** lists the whole plasma nitriding condition in this experiment.

The nitrided specimen was halved to prepare the test-pieces for SEM-EDX analyses. **Figure 8** depicts the cross-sectional SEM image as well as the nitrogen mapping from the surface to the depth of nitrided specimen. The nitrogen content is measured at the surface to be 9 mass% or 26 at%. The nitrided layer thickness reaches to be 66.5 μm.

Compared with **Table 2**, both the nitrogen solute content at the surface and the nitrided layer thickness become the highest by using this plasma nitriding at 673 K for 14.4 ks. Formation of

References	Treatment systems	Stainless steels	Temperature (K)	Time (h)	Nitrogen Surface Concentration (at%)	Nitrided Thickness (μm)
E. Menthe, 1999	DC Plasma Nitriding	AISI304L	723 K	5 h	22 at%	11 μm
Y. Sun, 1999	DC Plasma Nitriding	AISI304	673 K	5 h	14 at%	10 μm
W. Liang, 2000	Plasma Nitriding	AISI304	693 K	1.5 h	17 at%	10 μm
L. Wang, 2006	Plasma Nitriding	AISI304	693 K	44 h	-	27 μm
S. Lu, 2017	DC Plasma Nitriding	AISI304	673 K	8 h	-	51.7 μm

Table 2. Previous studies on the low temperature plasma nitriding of AISI304 stainless steels.

Parameter	Pre-Sputtering	Plasma nitriding
Temperature (K)	673	673
Pressure (Pa)	300	60
RF-Voltage (V)	250	250
DC-Voltage (V)	350	500
Gas Flow (ml/min)	160 N_2	160 N_2, 30 H_2
Gas ratio (%)	100 %N_2	84%N_2+16%H_2
Duration (sec)	1800	14400

Table 3. RF-DC high-density plasma nitriding conditions.

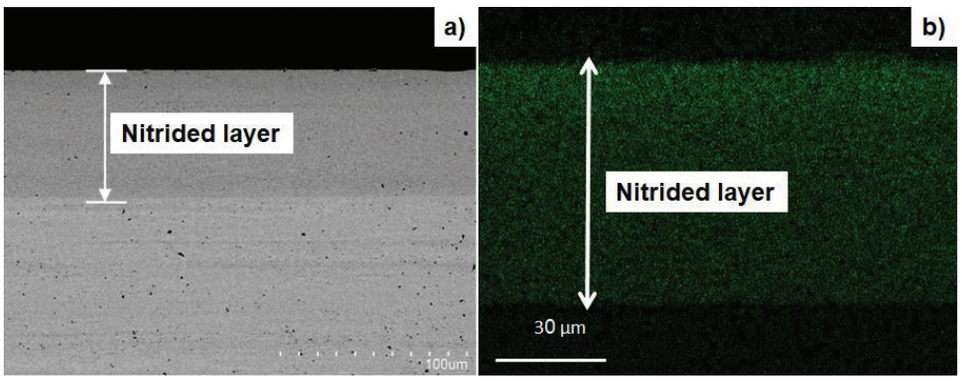

Figure 8. Cross-section of the plasma nitrided at 673 K for 14.4 ks. (a) SEM cross-sectional image and (b) nitrogen mapping from the surface to the depth.

uniform nitrogen super-saturated layer reveals that inner nitriding advances homogeneously into the depth of matrix.

3.3. Lattice expansion and elastic distortion

A nitrogen super-saturated lattice is expected to expand by itself; for example, the previous studies in **Table 2** reported a γ-lattice expansion by this nitrogen super-saturation. **Figure 9** compares the analyzed XRD diagrams before and after the plasma nitriding. The original austenitic phase is characterized by three peaks for γ (111), γ (200), and γ (220) detected at 2θ = 43.4, 50.82, and 74.5°, respectively.

Through the plasma nitriding process, all the austenitic lattices were elastically distorted to the expanded austenite (γ_N); for example, the original γ-peaks to AISI304 shifted to the lower 2θ, from 43.4 to 41.1°, from 50.82 to 47.94°, and from 74.5 to 70.08°, respectively. In parallel with these γ_N phases, the expanded martensitic peaks are also detected at 2θ = 43.7–63.5°. Negligibly small peak was detected at 2θ = 37.5° in trace level, which corresponds to the chromium nitrides. The γ-lattice expansion by this shift in XRD induces the tensile lattice strain by 5.4% for the peak shift from γ (111) to γ_N (111). This strain slightly increases to be

http://dx.doi.org/10.5772/intechopen.78365

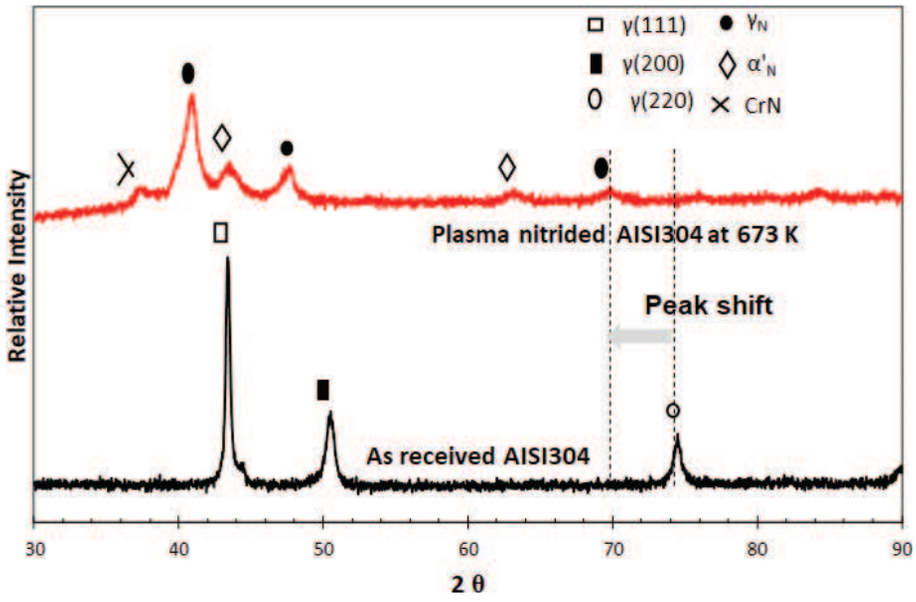

Figure 9. Comparison of analyzed XRD diagrams before and after plasma nitriding at 673 K.

5.6% for the shift of γ (200) to γ_N (200) and 5.4% for γ (220) to γ_N (220), respectively. This elastic distortion in the nitrogen super-saturated lattices just corresponds to the previous report in [41]. The grains housing these elastically distorted lattices are forced to deform plastically to compensate for strain incompatibility between the nitrogen unsaturated and the super-saturated lattices in grains.

3.4. Nitriding and hardening

EDX as well as the micro-Vickers testing are utilized to investigate the nitrogen content and hardness depth profiles. As depicted in **Figure 10**, the hardness becomes maximum at the

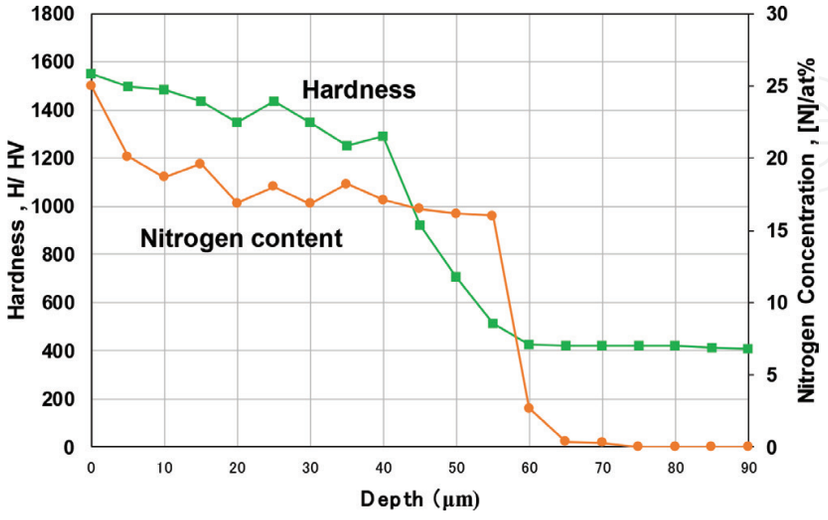

Figure 10. Nitrogen content and hardness depth profiles from the surface to the depth.

surface by 1550 HV and gradually reduces down to 1300 HV in the depth of d < 40 μm. From d = 40–66.5 μm, this hardness gradually decreases to the matrix hardness of 400 HV. A nitriding front-end is defined by the position in depth where the measured hardness coincides with the substrate hardness; the nitrided layer thickness (E) after nitriding for 14.4 ks is 66.5 μm. The nitrogen content is kept constant to be 15–17 at% in the depth of 5 < d < 60 μm except for the vicinities of surface and nitriding front-end. In the high temperature nitriding, the nitrogen content exponentially decays from the maximum nitrogen solubility limit of 0.1 mass% at the surface and goes to zero at the nitriding front-end. The nitrogen solute content depth profile in **Figure 10** is far from the common knowledge on the inner nitriding process in the high temperature nitriding.

3.5. Phase transformation and plastic straining

EBSD provides a tool to describe the interrelation among the phase transformation, the plastic straining, and the microstructure evolution. The measured phase mapping and KAM distribution on the cross-section of the nitrided specimen are shown in **Figure 11a** and **b**, respectively. After [42], the measured cross-sectional KAM profile can be identified as an equivalent plastic strain distribution.

In **Figure 11a**, the expanded γ-phase and transformed α′-phase finely distribute in the depth of d < 40 μm and form the two-phase microstructure. This homogeneous two-phase structure abruptly changes to a heterogeneous one where α′-phase sparsely distributes in the γ-phase matrix. This autonomous phase mapping change coincides with the onset of hardness reduction in **Figure 10**. This is because the volume fraction of extended γ-phase and transformed α′-phase zones begins to reduce from d = 40 μm in **Figure 11a**.

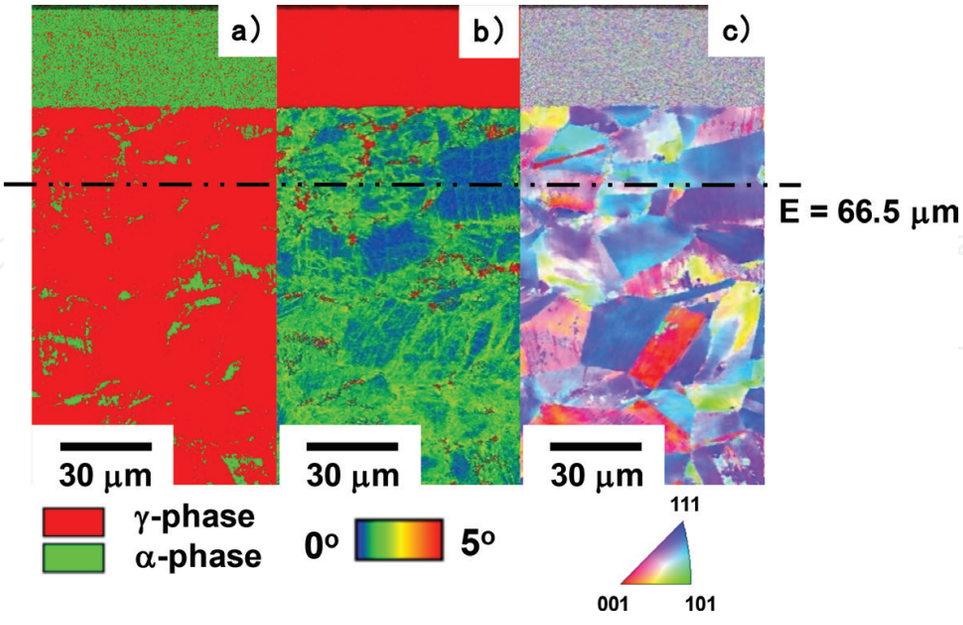

Figure 11. EBSD analysis on the cross-section of the nitrided AISI304 specimen at 673 K for 14.4 ks. (a) KAM distribution, (b) phase mapping, and (c) IPF depth profile.

http://dx.doi.org/10.5772/intechopen.78365

In **Figure 11b**, the layer of d < 40 μm is plastically strained in all since most of grains house the expanded lattice zones and plastically distort to compensate for the strain incompatibility in each grain. Just as seen in **Figure 11a**, this homogeneous plastic straining also changes by itself and localizes to specified grains. In fact, plastic strains localize in each grain below d = 40 μm. That is, uniform phase transformation and plastic straining change themselves across this critical depth by their localization to grains. The neighboring lattices to elastically distorted ones by phase transformation are forced to make plastic distortion. The transformed α'-phase zones in **Figure 11a** correspond to the highly strained zones in **Figure 11b**.

3.6. Microstructure refinement

Phase transformation and plastic straining in the above reflects the microstructure change by the nitrogen super-saturation. **Figure 11c** depicts the IPF distribution on the cross-section of the nitrided specimen. Each grain with a specified crystallographic orientation is represented by a different color. In correspondence to **Figure 11a** and **b**, the layer of d < 40 mm has refined microstructure with the average grains size of 0.1 μm, just near the spatial resolution of EBSD. This gray color for this layer in **Figure 11c** implies that each grain in this layer is homogeneously refined to have random crystallographic orientation. Just as observed in **Figure 11a** and **b**, this homogeneous microstructure changes by itself to heterogeneous one at d = 40 μm; the average grain size comes near to the original grain size before nitriding. To be noticed, the crystallographic orientations with different colors from original one or with graded colors are seen in most of the grains below d = 40 μm. The plastically strained grains are partially decomposed into several or tens of subgrains with different crystallographic orientations.

3.7. Summary

LTN of austenitic stainless steels is essentially different from the conventional plasma nitriding at higher temperatures. No nitrides are formed in the matrix so that no change in the original chromium content proves less change in the original corrosion resistance of stainless steels. The surface layer is hardened by nitrogen solid-solution where the γ-phase is expanded by nitrogen super-saturation with the occupation of octahedral vacancy sites by nitrogen solutes. Owing to fine grain size in the homogeneously nitrided layer, higher strength is expected to this high-nitrogen stainless steel surface. In addition, the fine-grained two-phase structure has a role to improve the trade-off-balancing between strength and fracture toughness and to increase the fatigue life [2]. How to extend this homogeneously nitrided layer toward the nitriding front-end must be an engineering issue to be discussed further.

4. Discussion

Inner nitriding mechanism in this low temperature plasma nitriding of austenitic stainless steels is discussed with importance on the difference between the homogeneous and heterogeneous nitriding processes.

4.1. Synergetic loop to drive the low temperature plasma nitriding

LTN mechanism is described by a synergetic loop as explained by **Figure 12**. Nitrogen solute, penetrating from the surface under high-nitrogen flux, occupies with an octahedral vacancy sites in the fcc-structured lattice as suggested by [43]. Under this nitrogen super-saturation, the γ-lattice expands, and elastically distorts to drive the γ to α' phase transformation. The whole γ-lattices neighboring to expanding γ-lattices and transformed α'-lattices, are plastically strained to compensate for the strain incompatibility between two zones. Original grain is distorted and decomposed into fine subgrains by this plastic straining. More nitrogen solutes diffuse to the depth of unsaturated matrix through the refined grain boundaries. Evolution of the nitrided layer accompanies with this loop.

4.2. Homogeneous nitriding process

When this synergetic loop is sustained during the plasma nitriding, every unit process uniformly advances from the surface to the depth of matrix. As seen in **Figure 11**, the original coarse-grained AISI304 matrix is surface-modified to have fine-grained, two-phase microstructure from the surface to the depth of 40 μm. This homogeneous nitriding is shut down at the critical depth of 40 μm for the nitrided AISI304 at 673 K for 14.4 ks in **Figure 11**; the above loop only takes place locally below this critical depth. There is no change in the synergetic loop across this criticality. When the loop works uniformly in the matrix, the nitriding advances homogeneously, while it does heterogeneously when the loop localizes in the selected grains. In other words, this autonomous change from heterogeneous nitriding to homogeneous nitriding is driven by the nitrogen super-saturation process into grains. When the nitrogen super-saturated γ-phase zones are closely neighboring to each other in the specified grain, the whole related grains are homogeneously nitrided and refined by the synergetic loop in **Figure 12**. On the other hand, when each super-saturated γ-phase zones are isolated from each other, every process in the loop works only inside of each grain.

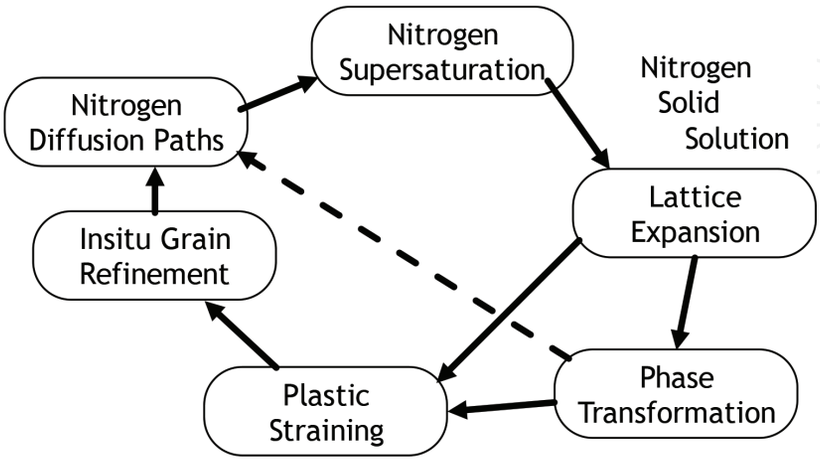

Figure 12. Synergetic loop of processing steps to drive the low temperature inner nitriding of stainless steels.

http://dx.doi.org/10.5772/intechopen.78365

4.3. Heterogeneous nitriding process

Let us first describe the localization of phase transformation, plastic straining, and micro-refinement below the critical depth in **Figure 11**. The phase mapping, the plastic strain distribution as well as the IPF mapping for the grain-A at d = 100 μm in **Figure 11** are analyzed and shown in **Figure 13**. Since a grain boundary works as a nitrogen diffusion path, most of the γ-phase zones at its vicinity transform to α′-phase. As pointed by an arrow-a in **Figure 13a** and **b**, a series of α′-phase zones are aligned in the alternate order of {- (α′-phase zone) − (highly plastic-strained zone) − (α′-phase) -}. In correspondence to this alignment, an original (001) orientation rotates by the plastic straining as shown in the graded colors in **Figure 11c**. The transformed zones have (111) orientation as pointed by arrow-b. This local change in phase mapping, plastic straining, and crystallographic orientation distribution in the inside of grain-A proves that the heterogeneous nitriding process is driven by this localization in each grain of matrix below the critical depth.

Figure 13 also suggests that each transformed band, pointed by the arrow-a, has a unit size of 0.3–0.5 μm in common and that these bands are isolated by highly strained γ-phase zones. With the enhancement of the nitrogen flux from the surface or with an increase of the nitrogen diffusion path density, those isolated zones overlap with each other to change the heterogeneous nitriding to the homogeneous nitriding. In other words, homogeneous nitriding mode prevails in the low temperature plasma nitriding process with higher activation of nitrogen flux from plasmas or with reduction of the initial grain size to a comparable level of transformed units in **Figure 13**.

4.4. Initial grain size effect on nitriding process

An initial grain size of AISI304 sheet is controlled to decrease by intense rolling with the reduction in thickness by 90 % to demonstrate this mode change from heterogeneous nitriding to

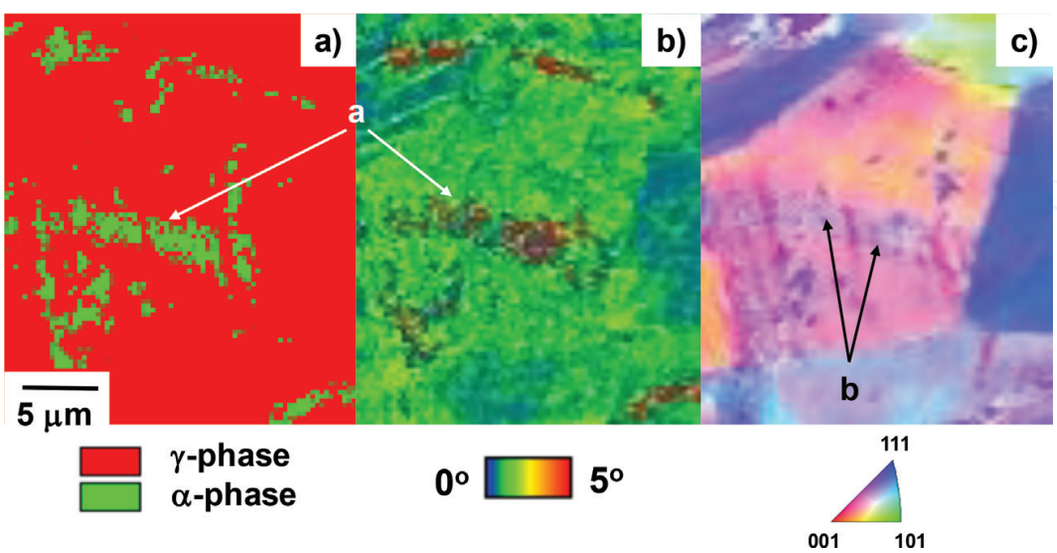

Figure 13. Localized steps around the grain-a in the heterogeneous nitriding process. (a) Local phase mapping, (b) local plastic straining, and (c) local IPF mapping.

homogeneous nitriding. **Figure 14** depicts the phase mapping, the plastic straining, and the microstructure refinement on the cross-section of rolled AISI304 before nitriding. Although crystallographic textures are formed along the rolling direction as shown by the arrow-a in **Figure 14**, the average grain size is uniformly reduced down to 1.5 μm.

Under the same processing conditions, this fine-grained AISI304 specimen is nitrided at 673 K for 14.4 ks. The nitriding front-end is analyzed to be E = 60 μm, nearly the same as shown in **Figure 11**. **Figure 15** shows the phase mapping, the plastic strain distribution, and the microstructure after nitriding. The heterogeneous microstructure observed above the nitriding front-end as well as the textures by rolling in **Figure 14**, completely disappears to form two-phase and fine-grained homogeneous nitrided layer. Although the initial fully martensitic phase turns to be $\gamma - \alpha'$ two-phase; this two-phase fine microstructure is continuously formed across the nitriding front-end. This homogenization of the heterogeneous microstructure reveals that nitrogen super-saturation process advances homogeneously into the depth of stainless steel matrix under the synergetic loop once the grain size of the matrix is comparable to the nitrogen super-saturated unit size.

4.5. Summary

LTN of stainless steels is essentially governed by the homogeneous nitrogen super-saturation. When the synergetic loop is sustained during the nitriding, the nitrided layer has two-phase, fine-grained microstructure. Once the nitrogen super-saturation process is localized into the specified grains, the homogeneous nitriding changes itself to heterogeneous nitriding.

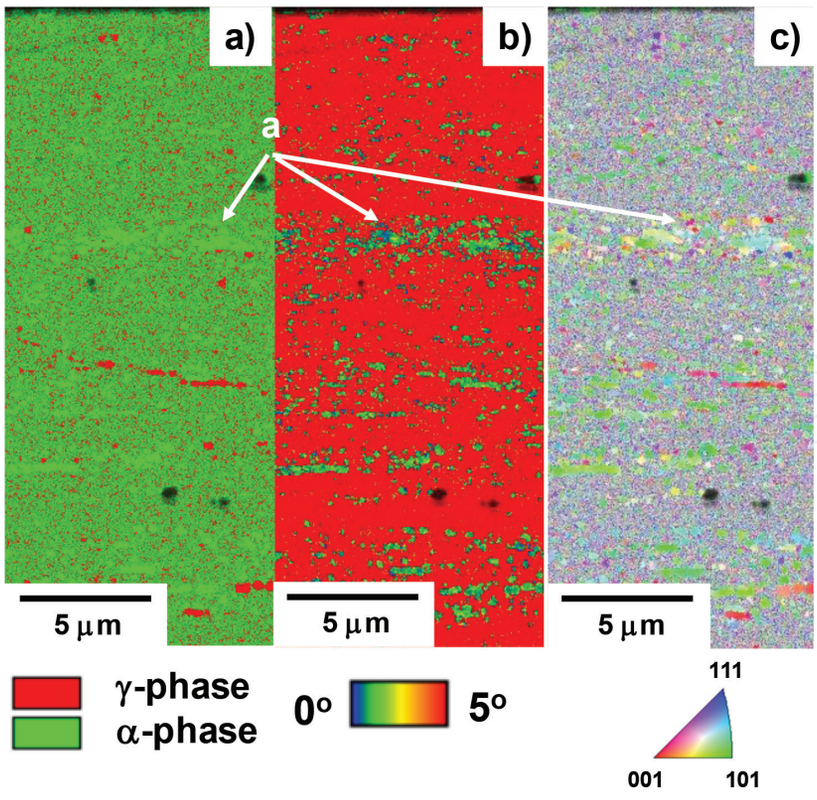

Figure 14. Microstructure of intensely rolled AISI304 sheet with the reduction of thickness by 90%. Average grain size is 1.5 μm.

http://dx.doi.org/10.5772/intechopen.78365

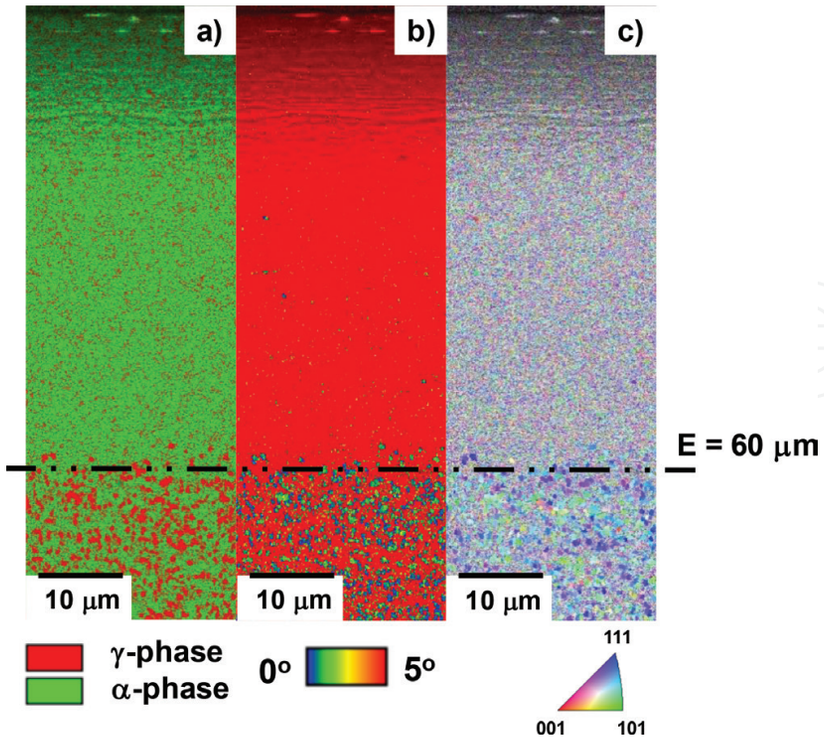

Figure 15. Microstructure after nitriding the fine-grained AISI304 at 673 K for 14.4 ks.

Refinement of the initial grain size into a comparable size of nitrogen saturated γ-lattice units homogenizes the heterogeneously nitrided layer.

5. Conclusion

Low temperature plasma nitriding provides a processing tool for the surface treatment of the stainless steels to have a fine two-phase microstructure with the average grain size of 0.1 μm. This homogeneously nitrided layer has higher surface hardness than 1500 HV and higher nitrogen content than 15 at%. Different from the conventional nitriding, (1) no nitrides are formed as a precipitate in the matrix, (2) stainless steel matrix is nitrogen super-saturated to have a nitrogen content plateau of 15–17 at% toward the nitriding front-end, (3) phase transformation and plastic straining take place together with γ-lattice expansion, and (4) original coarse grains are refined. This homogeneous nitriding follows the heterogeneous nitriding process where γ-lattice expands locally in the specified grains with phase transformation to α'-phase and plastic straining. When nitriding the fine-grained stainless steels, their surfaces are homogeneously nitrided to have fine, a two-phase microstructure with high hardness, strength, and corrosion resistance.

Acknowledgements

The author would like to express his gratitude to Mr. Abdelrahman Farghali (SIT) and late Mr. Y. Sugita (YS-Electric Industry, Co. Ltd.) for their help in experiments. This study was

financially supported in part by the Abe-Initiative in Japan Government and the METI-program on the supporting industries, Japan, respectively.

Conflict of interest

No conflicts of interest were declared.

Author details

Tatsuhiko Aizawa[1,2]*

*Address all correspondence to: taizawa@sic.shibaura-it.ac.jp

1 Shibaura Institute of Technology, Tokyo, Japan

2 Surface Engineering Design Laboratory, LLC, Tokyo, Japan

References

[1] Massalski TB, editor. Binary Alloy Phase Diagrams, Volume 2. Handbook on Phase Digrams. 2nd ed. ASM International; 1990. p. 1728

[2] Imai Y, Izumiyama M, Tsuchiya M. Thermodynamic study on the transformation of austenite into martensite in iron-high nitrogen and iron carbon binary system. Journal of the Japanese Institute of Metals and Materials. 1965;**29**:427-435

[3] Bell T, Owen WS. Journal of the Iron and Steel Institute. 1967;**205**:428

[4] Gavriljuk V et al. In: Proceedings of 1st High Nitrogen Steels; Lilly; 1988. p. 447

[5] Murata I, Sakamoto M. Properties of High Nitrogen Steels. Agune; 2005. pp. 166-168

[6] Katada Y. Outlook 2006 of National Institute of Materials Sciences. Tsukuba: National Institute of Materials Sciences; Cap3-5-72006. pp. 342-345

[7] Komuro M, Kozono Y, Hanazono M, Sugita Y. Structure and saturation magnetic flux density of epitaxially grown Fe and Fe-N films on GaAs (100). 1989;**13**(2):301-306

[8] W Holzgruber. 1974. Austrian Patent No. 333327, S12

[9] Stein G, Menzel J, Dorr H. In: Foct J, Hendry A, editors. High Nitrogen Steels HNS88. London: Maney Publishing; 1988. p. 32

[10] Berns H, Kühl A. Reduction in wear of sea page pump through solution nitriding. Wear. 2004;**246**:16-20

[11] Aizawa T, Sugita Y. High density RF-DC plasma nitriding of steels for die and mold technologies. Research Report. SIT. 2013;**57**(1):1-10

[12] Aizawa T, Sugita Y. High density plasma nitriding of tool and die steels. In: Proceedings of the 6th South East Asian Technical University Consortium Symposium; 2012. pp. 134-137

[13] Kuwahara H. Surface modification of iron alloys by plasma nitriding and carburizing [PhD Thesis]. Kyoto University; 1992

[14] Hiraoka Y, Inoue K. Prediction of nitrogen distribution in steels after plasma nitriding. Denki-Seiko. 2010;**86**:15-24

[15] Granito N, Kuwahara H, Aizawa T. Normal and anormal microstructure of plasma nitrided Fe-Cr alloys. Journal of Materials Science. 2002;**37**(4):835-844

[16] Bell T. Surface engineering of austenitic stainless steel. Surface Engineering. 2002;**18**: 415-422

[17] Dong H. S-phase surface engineering of Fe-Cr, Co-Cr and Ni-Cr alloys. International Materials Reviews. 2011;**55**(2):65-98

[18] Saito K. Introduction to Ion Nitriding in Hokunetsu. 2018. p. 3. http://hokunetsu.com/products/003/

[19] Gruen P. PulsePlasma@. Broacher of PlaTeg; 2008

[20] Granto N. Surface material design and control in steels for automotive parts by plasma nitriding technique [PhD thesis]. University of Tokyo; 2003

[21] Marcos G, Guilet S, Cleymand F, Thiriet T, Czerwiec T. Stainless steel patterning by combination of micro-patterning and driven strain produced by plasma assisted nitriding. Surface and Coatings Technology. 2011;**205**:5275-5279

[22] Aizawa T, Fukuda T, Itoh K. Duplex coating of AISI316 and 420 dies for holt mold-stamping. Journal of Iron and Steel International. 2012;**219**:933-936

[23] Katoh T, Aizawa T, Yamaguchi T. Plasma assisted nitriding for micro-texturing onto martensitic stainless steels. Manufacturing Review. 2015;**2**:2, 1-7

[24] Aizawa T, Fukuda T, Itoh K. Duplex coating of AISI-316 and 420 dies for hot mold-stamping. Steel Research International Journal. 2012;**212**:933-936

[25] Istiroyah, Aizawa T, Santjojo DJ. High density plasma nitriding behavior of austenitic stainless steel type AISI 316. In: Proceedings of the 7th SEATUC Conference; Bandon; 2013 (CD-ROM)

[26] Djoko DJ, Aizawa T. Formation of expanded martensite in plasma nitrided AISI420 stainless steel. In: Proceedings of the 8th SEATUC Conference; Johor-Balu; 2014 (CD-ROM)

[27] Yunata EE. Characterization and application of hollow cathode oxygen plasma [PhD thesis]. SIT; 2016

[28] Rosadi I, Djoko S, Sakti SP, Yunata EE, Aizawa T. Plasma diagnosis on the mixture gas plasma states for nitriding and surface activation. In: Proceedings of the 12th SEATUC Conference; Yogyakarta, Indonesia; 2018 (in press)

[29] Santjojo D, Itsiroyah, Aizawa T. Dynamic of nitrogen and hydrogen species in a high rate plasma nitriding of martensitic stainless steels. In: Proceedings of the 9th SEATUC Conference; Thai; 2015 (CD-ROM)

[30] Yunata EE, Aizawa T, Santojojo DJ. Characterization of hollow cathode plasma for ashing processes. In: Proceedings of the 8th SEATUC Conference; Johor-Balu; 2014 (CD-ROM)

[31] Menthe E, Rie K-T. Further investigation of the structure and properties of austenitic stainless steel after plasma nitriding. Surface and Coatings Technology. 1999;**116**:199-204

[32] Sun Y, Li XY, Bell T. X-ray diffraction characterization of low temperature plasma nitrided austenitic stainless steels. Journal of Materials Science. 1999;**34**:4793-4802

[33] Liang W, Xiaolei X, Bin X, Zhiwei Y, Zukun H. Low temperature nitriding and carburizing of AISI304 stainless steel by a low pressure plasma arc source. Surface and Coatings Technology. 2000;**131**:563-657

[34] Wang L, Ji S, Sun J. Effect of nitriding time on the nitrided layer of AISI 304 austenitic stainless steel. Surface and Coatings Technology. 2006;**200**:5067-5070

[35] Lu S, Zhao X, Wang S, Li J, Wei W, Hu J. Performance enhancement by plasma nitriding at low gas pressure for 304 austenitic stainless steel. Vacuum. 2017;**145**:334-339

[36] Aizawa T. Functionalization of stainless steels via low temperature plasma nitriding. In: Proceedings of the 7th Annual Basic Science International Conference; Malang, Indonesia; 2017. pp. 1-16

[37] Farghali A, Aizawa T. Phase transformation induced by high nitrogen content solid solution in the martensitic stainless steels. Materials Transactions. 2017;**58**:697-700

[38] Farghali A, Aizawa T. Nitrogen supersaturation process in the AISI420 martensitic stainless steels by low temperature plasma nitriding. ISIJ International. 2018;**58**(3):401-407

[39] A. Farghali, T. Aizawa, Homogeneous and Heterogeneous Structuring Processes in the Nitrided Austenitic Stainless Steels below 673K. Materials Science and Engineering, (2018) (in press)

[40] Aizawa T, Yoshihara S. Homogeneous and heterogeneous micro-structuring of austenitic stainless steels by the low temperature plasma nitriding. In: Proceedings of 7th International Conference on Material Strength and Applied Mechanics; Kita-Kyushu, Japan; 2018 (in press)

[41] Öztürk O, Williamson DL. Phase and composition depth distribution analyses of low energy, high flux N implanted stainless steel. Journal of Applied Physics. 1995;**77**: 3839-3850

[42] Kamaya M, Wilkinson AJ, Titchmarsh JM. Quantification of plastic strain of stainless steel and nickel alloy by electron backscatter diffraction. Acta Materialia. 2006;**54**:539-548

[43] Domain C, Becquart CS, Foct J. Ab initio study of foreign interstitial atom (C, N) interactions with intrinsic point defects in α-Fe. Physical Review B. 2004;**69**:144122